# *IN SILICO* MODELING OF MURINE MUSCLE DISUSE ATROPHY

Yasmina Zeineddine[1], Silvia Blemker, Ph.D.[1]

Department of Biomedical Engineering, University of Virginia, Charlottesville, VA, USA[1]

## Abstract

Spaceflight-induced disuse atrophy of postural skeletal muscle remains a major barrier to long-duration human exploration. Current exercise and nutritional countermeasures do not fully prevent muscle loss. To investigate mechanisms underlying this response, we developed an agent-based model (ABM) of murine skeletal muscle in CompuCell3D. The model integrates extracellular signals including mechanical load, insulin-like growth factor-1 (IGF-1), amino acid availability, and myostatin signaling to regulate muscle protein synthesis (MPS), muscle protein breakdown (MPB), and fiber cross-sectional area (CSA). The model represents a segmented murine gastrocnemius cross-section containing 132 muscle fibers of four types (I, IIA, IIX, and IIB). Calibration was performed using Latin Hypercube Sampling and the CaliPro framework against seven murine gastrocnemius cohorts spanning 1-30 days. The accepted parameter space reproduces fiber-type specific atrophy trajectories, maintains homeostasis within a 10% drift threshold, and predicts a 57% reduction in simulated muscle-wide fractional synthesis rate during disuse. Sensitivity analysis further suggested that homeostatic fiber size is governed primarily by myostatin and amino acid sensitivity, whereas atrophy severity is strongly influenced by basal MPS. Together, these results support MPS suppression as a major contributor to disuse atrophy and establish this model as a foundation for mechanistic testing of spaceflight countermeasures.

## Introduction

Spaceflight-induced disuse atrophy of postural (anti-gravity) muscles presents a significant hurdle to long-duration human spaceflight. Skeletal muscle mass loss in microgravity compromises functional capacity, increases injury risk, and disrupts metabolic regulation.[1–6] Given that muscle mass and strength correlate directly with mortality and health outcomes in both clinical and healthy populations,[7,8] progressive muscle loss in astronauts has direct implications for mission safety and crew longevity. As the Artemis missions prepare us for a return to the Moon, and missions to Mars draw closer, astronauts will be required to perform physically intensive tasks, such as extravehicular walks in hypo- and microgravity environments. Thus, preservation of muscle mass and function is essential for mission success.

Current in-flight mitigation strategies revolve around exercise and nutritional supplementation, particularly protein ingestion. Despite adherence to these protocols, astronauts remain susceptible to losing 10-30% of lower limb muscle mass.[9–11] These data demonstrate that current guidance fails to fully address root causes of spaceflight atrophy and reflects an incomplete mechanistic understanding of how microgravity disrupts muscle homeostasis.

Skeletal muscle mass is regulated by the dynamic balance between protein synthesis (MPS) and breakdown (MPB).[12] Previous research identifies MPS suppression as a major driver of disuse atrophy, with MPS rates falling 40-70% in both rodent and human unloading models.[13,14] Upstream regulators of

MPS include mechanotransduction through integrin signaling, focal adhesion kinases, and stretch-activated channels[15]; insulin-like growth factor-1 (IGF-1) signaling through the PI3K/Akt pathway; and amino acid availability, all of which converge on the mTOR pathway,[16] a central regulator of cell growth. MPB is mediated through three major proteolytic systems: the ubiquitin-proteasome pathway, calpain-mediated proteolysis, and lysosomal autophagy. These catabolic pathways are activated by myostatin/activin signaling, inflammatory cytokines, nutrient deprivation, and altered mechanical loading.[17]

In microgravity, postural muscles of the lower limbs and trunk undergo a rapid transition from continuous gravitational loading to near-zero mechanical tension, removing a dominant anabolic stimulus. This is compounded by the development of anabolic resistance, a state in which muscle fibers exhibit blunted responsiveness to both exercise and amino acids.[18,19] The complex interactions between mechanical signal loss, anabolic resistance, and upregulations in catabolic signaling likely limits single-target interventions against muscle atrophy. For example, IGF-1 overexpression fails to protect muscle mass during hindlimb unloading.[20,21]

Dissecting these interacting mechanisms experimentally is challenging because disuse studies are costly, time-intensive, and often unable to capture tissue-level spatiotemporal signaling dynamics. Computational modeling provides a complementary framework for addressing these gaps. Agent-based models (ABMs) simulate biological systems by assigning rule-based behaviors derived from experimental data to individual cellular agents. This approach allows tissue-level phenomena to emerge from local interactions and offers a platform for mechanistic interrogation, hypothesis testing, and prediction of responses to perturbations that are difficult to isolate experimentally.

Here, we present the development and partial calibration of a murine skeletal muscle ABM designed to investigate the mechanisms underlying spaceflight-induced muscle atrophy. The model was built using the CompuCell3D Cellular Potts[22] framework. It functions through fiber-type specific protein turnover dynamics and signal integration of mechanical load, IGF-1, amino acids, and myostatin to predict changes in normalized muscle fiber cross-sectional area (CSA) over 30 days of simulated microgravity. The model was calibrated against gastrocnemius hindlimb unloading data using Latin Hypercube Sampling and the CaliPro[23] parameter estimation method. This progress report describes the model architecture, calibration approach, and preliminary results.

## Methods

The model was developed in CompuCell3D (CC3D) version 4.4.1,[22,24] a Cellular Potts framework in which biological cells are represented as collections of lattice sites whose configurations evolve through stochastic energy minimization. The simulation lattice (340x366 pixels, 2 μm per pixel) represents a manually segmented[25] cross-section containing 132 muscle fibers with a total tissue area of 0.3mm$^2$. At initialization, lattice pixels are assigned to muscle fibers, capillaries, or extracellular matrix (ECM).

Four skeletal muscle fiber types are represented: Type I (slow-twitch oxidative), Type IIA (fast-oxidative), Type IIX (fast/intermediate glycolytic), and Type IIB (fast-glycolytic). These fiber types were included because differential fiber-type atrophy is a hallmark of disuse atrophy,[26,27] a byproduct of differential fiber type sensitivity to anabolic and catabolic stimuli. [26–29] Fiber type composition is assigned at initialization using murine gastrocnemius proportions (Type I: 9.2%, Type IIA: 15.6%, Type IIX: 24.2%, Type IIB: 51.0%).[32] Capillaries were

initialized from ECM cells at a capillary:fiber ratio of 1.5:1.[33] Capillaries secrete amino acids into the surrounding field once per simulated hour (4 Monte Carlo Steps of 15 min each), representing continuous amino acid delivery to muscles under fed conditions. Muscle fibers secrete, uptake, and respond to IGF-1 and myostatin. Signal diffusion coefficients were calculated as described here.[24,34]

Fiber Size Dynamics

Fiber cross-sectional area (CSA) is governed by the balance between MPS and MPB, which can be modeled using a first order turnover equation:

$$\frac{dCSA}{dt} = MPS - MPB * CSA \quad (1)$$

Where MPS is absolute protein synthesis (pixels day$^{-1}$ and MPB is the effective fractional protein rate (day$^{-1}$). This formulation yields a stable equilibrium at CSA=MPS/MPB.[35] CSA updates every simulated hour and gets passed to the Cellular Potts energy-minimization routine to drive fiber configurations. The lag captures delays between upstream signaling and measurable changes in protein turnover while preserving numerical stability.

Anabolic Signal Integration

Four extracellular signals regulated MPS in the model: mechanical load (MECH), IGF-1, amino acids (AA) and myostatin (MSTN). Each signal was converted into a dimensionless activation term using a saturating Hill-type equation:

$$S_i = \frac{C_i}{C_i + K_i} \quad (2)$$

Where $C_i$ is the local concentration sensed by a fiber and $K_i$ is the half-saturation constant for that signal that determines the sensitive operating region. The loading parameter was set to 1.0 under normal loading and 0.1 under unloading, representing the 8-12% drop in electromyographic activity of the gastrocnemius observed during disuse.[36]

The net anabolic drive was calculated using a weighted combination of anabolic inputs modulated by myostatin inhibition:

$$drive = \left(\frac{W_{IGF} * sig_{IGF} + W_{MECH} * sig_{MECH} + W_{AA} * sig_{AA}}{W_{IGF} + W_{MECH} + W_{AA}}\right) * (1 - sig_{MSTN} * W_{MSTN}) \quad (3)$$

$w_{MECH}$, $w_{AA}$, and $w_{MSTN}$ are fiber-type-specific sensitivity weights chosen to reflect published differences in MPS response to each signal across fiber types.[28,29,31,37]

Fiber-specific MPS was then calculated as:

$$MPS = base\_MPS_{ft}[(basal_{frac} + (1 - basal_{frac}) * drive] * AR(t)] \quad (4)$$

where base_MPS$_{ft}$ is the fiber-type specific homeostatic synthesis rate, basal_frac is the constitutive synthesis fraction that maintains basal protein turnover in the absence of anabolic signaling, and AR(t) is a time-varying anabolic resistance term. Published studies suggest that baseline MPS differs across fiber types, with Type IIA fibers exhibiting the highest basal MPS,[28,29] the model uses MPS_IIA as the reference basal synthesis parameter. Basal MPS values for Types I, IIX, and IIB are scaled relative to this parameter using literature-based fiber-type differences (I=0.95IIA, IIX=0.8IIA, IIB=0.68IIA). This preserves biologically motivated turnover

hierarchy while reducing the dimensionality of the free parameter space.

AR is modeled as an exponentially decaying coefficient with a floor (50%):

$$AR(t) = \max\left(AR\_floor, e^{-\lambda t}\right) \quad (5)$$

Where t is simulation time and λ is the decay constant controlling rate of anabolic resistance development. To reach the AR_floor by day 5, λ was set to 0.0033, matching experimental timelines.[18,19,38]

Catabolic Signal Integration

Effective MPB for each fiber was modulated by amino acid availability and mechanical loading, as feeding and loading both depress MPB.[39,40] Since initialized fibers span a large CSA range, a uniform basal MPB would lead to CSA drift. To ensure that fiber size dynamics start under homeostatic conditions, $MPB_{base}$ is derived analytically for each fiber at initialization:

$$MPB_{base} = \frac{MPS_{homeo}}{MPB_{homeo} * CSA_0} \quad (6)$$

where $MPS_{homeo}$ is the effective synthesis rate evaluated at expected homeostatic signal levels, $MPB_{homeo}$ the product of the suppressive breakdown terms under homeostatic conditions (Eq. 7), and $CSA_0$ is the initial CSA of the fiber. This initialization guarantees $\frac{dCSA}{dt} = 0$ at $t = 0$ for every fiber and reduces the number of independently swept turnover parameters, since breakdown is derived from synthesis and initial fiber size rather than calibrated independently. $MPB_{base}$ is then used to calculate changes in effective MPB:

$$MPB_{eff} = MPB_{base}(1 - MPB_{AA}S_{AA}) * (1 - MPB_{MECH} * S_{MECH}) \quad (7)$$

Calibration

Model calibration followed the CaliPro framework,[23] in which Latin Hypercube Sampling is used to efficiently explore multidimensional parameter spaces. Sampled runs are classified as pass/fail using user-defined criteria based on experimental data. Calibration was performed against seven murine gastrocnemius unloading cohorts spanning 1–30 days[41–47] and including hindlimb suspension, spaceflight, and immobilization datasets. Homeostasis (Loading = 1) and atrophy (Loading = 0) were evaluated separately using paired simulations of the same parameter set.

Calibration has been performed across six sweeps to date. In each sweep, 250 unique parameter sets with 3 replicates per run were generated by LHS and evaluated under both loaded and unloaded conditions, corresponding to 750 sampled parameter sets per sweep. Acceptance rates increased across successive sweeps, progressing from 0 accepted sets in the earliest sweep, to 5/250 in a later sweep, to 138/250 (55.2%) in the current sweep.

Thirteen free parameters were sampled in each run, including signal half-saturation constants ($K_{IGF}$ , $K_{AA}$ , $K_{MSTN}$), reference basal protein synthesis term MPS_IIA, MPB suppression weights ($MPB_{MECH}$ , $MPB_{AA}$), decay constants for the three field signals, and amino acid secretion from capillaries (AASecretionCap). Parameters spanning multiple orders of magnitude were sampled logarithmically.

Simulation outputs were stored per run as fiber-level time series and summary field trajectories. Outputs include normalized CSA,

MPS rate, MPB rate, and signal values. Literature-derived experimental data were normalized to day 0 within study-specific cohorts and aggregated by fiber type and day to produce target calibration envelopes.

A parameter set was accepted only if the loaded simulation remained within a 10% homeostatic drift threshold and the matched unloading simulation remained within the calibration envelopes at each timepoint. Envelopes were defined as scalar multiples of the minimum and maximum experimental values observed at each calibration day. Early sweeps used broad envelopes spanning 0.5× the minimum to 2× the maximum observed value, allowing a wide range of behaviors to be sampled. The current sweep uses tighter envelopes spanning 0.9× the minimum to 1.1× the maximum, approximating the raw experimental range. Runs that failed these criteria were penalized, and the resulting pass/fail structure was used to guide iterative narrowing of parameter ranges in a CaliPro-style workflow. Passing parameter sets were further analyzed using Alternative Density Subtraction and Highest Density Region summaries to identify productive regions of parameter space for the next sweep.

**Table 1.** A list of parameters, fixed and calibrated for the model. The parameter function, starting range, and accepted range are shown.

| Parameter | Purpose | Start Range | Current Range |
|---|---|---|---|
| MPS_IIA | Basal reference IIA MPS, scales other MPS rates | (0.01 – 100) | 20-60 |
| K_IGF | Half-saturation constant for IGF-1 | 0.05-10000 | 200-300 |
| K_AA | Half saturation constant for amino acids | 0.05-10000 | 0.001-0.5 |
| K_MSTN | Half saturation constant for myostatin | 0.05-10000 | 0.9-1.5 |
| IGFdecay | Decay constant for IGF-1 | 0.0001-0.5 | 0.14-0.2 |
| AAdecay | Decay constant for amino acids | 0.0001-0.5 | 0.2-0.35 |
| Myostatindecay | Decay constant for myostatin | 0.0001-0.5 | 0.1-0.25 |
| MPB_MECH | Strength of load-mediated MPB suppression | 0.01-0.9 | 0.01-0.05 |
| MPB_AA | Strength of amino acid-mediated MPB suppression | 0.01-0.9 | 0.01-0.05 |
| Basal_frac | Constitutive synthesis fraction that maintains basal MPS independent of anabolic drive | 0.001-0.5 | 0.01-0.05 |
| AASecretionCap | Amino acid secretion rate from capillaries | 1-100 | 15-20 |
| $W_{MSTN}$ | Fixed MSTN weight, 30% basal MPS suppression | 0.6 | |
| Type I weights: $W_{MECH}$, $W_{IGF}$, $W_{AA}$ | Fixed signal weights, data-derived from inhibition or delivery studies that measured changes in MPS | 1.0; 0.45; 0.56 | |
| Type IIA weights: $W_{MECH}$, $W_{IGF}$, $W_{AA}$ | | 1.0; 0.5; 0.64 | |
| Type IIX weights: $W_{MECH}$, $W_{IGF}$, $W_{AA}$ | | 0.9; 0.76; 0.64 | |
| Type IIB weights: $W_{MECH}$, $W_{IGF}$, $W_{AA}$ | | 0.7; 0.8; 0.9 | |

## Sensitivity Analysis

Sensitivity analysis was performed using Partial Rank Correlation Coefficients (PRCCs). PRCCs were calculated separately for each fiber type and loading condition using final normalized CSA as the primary output. PRCC was computed on ranked parameter and outcome values while controlling for the influence of the other sampled parameters, allowing identification of fiber-type specific relationships within the current accepted parameter space.

## Results

Calibration identifies a productive parameter space for homeostasis and disuse

Model calibration was performed using the CaliPro framework across six iterative sweeps. In each sweep, 250 unique parameter sets were generated using Latin hypercube sampling and evaluated under both homeostatic (Loading = 1) and atrophy (Loading = 0) conditions, and each run gets replicated three times, as the model is stochastic. This corresponds to 750 sampled parameter sets per sweep. Acceptance improved progressively across sweeps, beginning with zero accepted parameter sets, increasing to 5/250 in a later sweep, then reaching 138/250 (55.2%) in the most recent sweep. This progression indicates that iterative narrowing of the parameter space is increasing the density of parameter combinations consistent with experimental observations.

At the current calibration stage, the accepted parameter space is productive but not yet fully converged. Accordingly, the results below describe the behavior of a partially calibrated model rather than a final parameter set. Homeostatic runs were required to remain within a 10% drift threshold, while matched unloading runs were required to remain within the experimental calibration envelopes across the selected timepoints. The current accepted region therefore captures both stable maintenance under loaded conditions and robust atrophic behavior under unloading.

Figure 1 shows a section of the model lattice before and after 28 days of simulated unloading, illustrating a visible reduction in fiber CSA across fiber types.

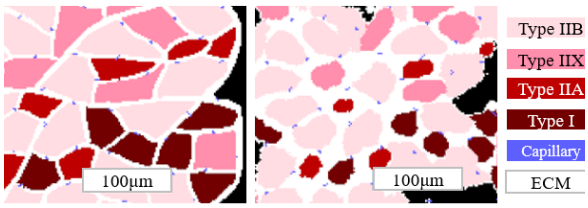


**Figure 1.** Muscle atrophy demonstrated in model lattice after 28 days of simulated disuse in the murine gastrocnemius.

The accepted parameter space reproduces fiber-type specific atrophy trajectories

The model produces fiber-type-specific atrophy trajectories consistent with calibration targets (Fig. 2). Type I and IIA fibers exhibit that largest normalized CSA losses, followed by Type IIX and IIB, mirroring the slow-twitch predominant atrophy pattern reported in both rodent and human studies.[26,27] This rank ordering emerged from the signal integration architecture developed for the model rather than direct assignment, providing an early indication of the model's ability to capture features of disuse biology.

Among the experimental fiber-type-specific mean values, 10% fell within the simulated 5th–95th percentile band of the accepted parameter space, indicating that the current calibrated region does not yet fully capture the magnitude of observed atrophy. The simulated trajectories consistently underestimate the degree of CSA loss relative to experimental means, producing a global upward offset that is uniform across fiber types rather than fiber-type-specific. Agreement was strongest from days 1–14, where the calibration dataset is most densely populated. Beyond day 14, confidence intervals widened due to scarcity of long-term fiber-type specific gastrocnemius data rather than obvious instability in the accepted simulations. Published datasets also show substantial inter-study variability arising from differences in mouse strain, age, sex, and unloading method. Additional longitudinal fiber-type specific datasets, particularly

beyond day 14, should further tighten calibration bounds and improve the precision of accepted parameter ranges.

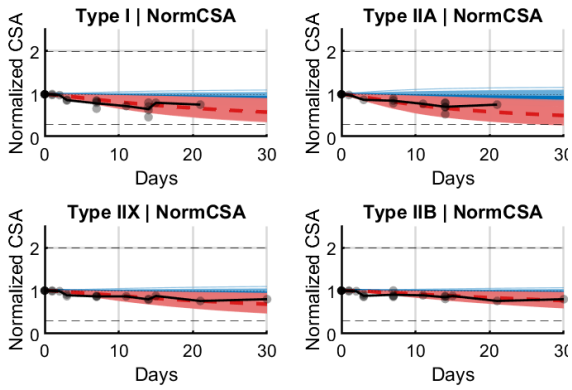


**Figure 2.** Fiber-type specific trajectories of disuse atrophy and homeostasis compared to experimental data. Red lines are atrophy runs, blue are homeostatic, black dots are experimental murine gastrocnemius, fiber-type specific CSA data.

## Sensitivity analysis reveals distinct regulators of homeostasis and atrophy

To identify which parameters most strongly correlate with final normalized CSA, PRCC analysis (Fig 3.) was conducted for each fiber type under both disuse and homeostatic conditions using day 28 normalized CSA as the primary outcome. A notable result was the separation between parameters that dominated fiber size under homeostasis and those that dominated fiber loss during unloading.

Within the current accepted parameter space, $K_{MSTN}$ showed the largest positive PRCC across fiber types under homeostatic conditions, indicating that the myostatin half-saturation constant is a major determinant of basal fiber size. Higher $K_{MSTN}$ reduces effective myostatin sensitivity, thereby decreasing suppression of MPS. In contrast, higher $K_{AA}$ was associated with lower final CSA, consistent with weaker amino acid signaling and reduced anabolic drive. Together, these results support the interpretation that myostatin and amino acid sensitivity are major regulators of muscle fiber size under loaded conditions.

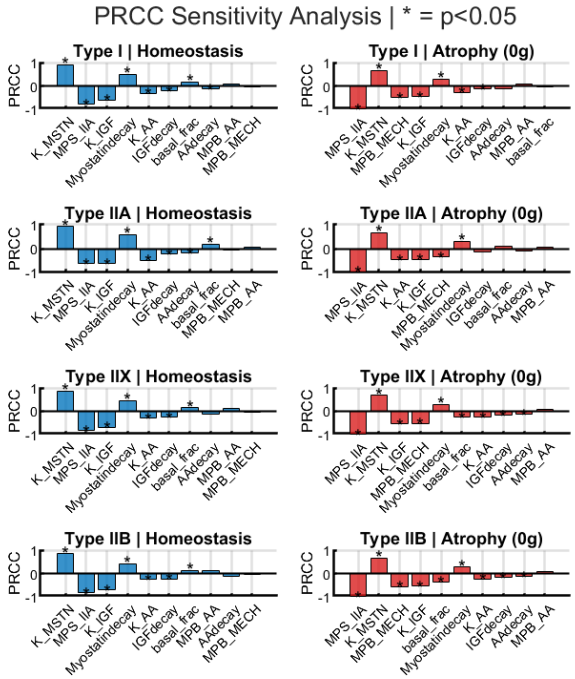


**Figure 3.** Partial Rank Correlation Coefficients by fiber type and loading condition reveal different drivers of homeostasis and atrophy.

This pattern shifted under unloading. In atrophy simulations, $MPS_{IIA}$, the reference basal synthesis parameter from which the other fiber-type MPS rates are scaled, emerged as one of the strongest regulators of atrophy severity across all fiber types. This finding is consistent with the hypothesis that higher baseline turnover architecture, which is represented most strongly in Type I and Type IIA fibers, can produce greater net fiber loss when anabolic drive is withdrawn. $MPB_{MECH}$ also displayed strong PRCC values, highlighting the importance of normal loading in suppressing breakdown and demonstrating how loss of load amplifies net catabolic balance. The dissociation between dominant parameters in loaded versus unloaded conditions suggests that mechanisms regulating baseline fiber size are not identical to those governing preservation of mass during disuse.

Simulated disuse atrophy is driven primarily by MPS suppression

Time-series outputs of MPS and MPB confirmed that atrophy in the current model is driven primarily by suppression of MPS rather than by large elevations in MPB. Tissue-wide fractional synthesis rate (FSR) was calculated as MPS normalized to fiber CSA and expressed as %/day (Fig. 4). Under homeostatic conditions, simulated FSR was approximately 3.5%/day, whereas under unloading it fell to approximately 1.5%/day, corresponding to an approximately 57% reduction. These values are consistent with published murine and human unloading studies reporting 40–60% declines in synthesis within the first two weeks of disuse. [18,19,48,49]

In contrast, MPB increased only modestly during simulated atrophy, rising by approximately 3–5% across fiber types over the course of unloading. This pattern supports the mechanistic interpretation that loss of anabolic drive and development of anabolic resistance are sufficient to explain much of the observed atrophy trajectory in the current model. It also indicates that the present framework can reproduce experimentally consistent turnover dynamics without requiring large sustained increases in breakdown.

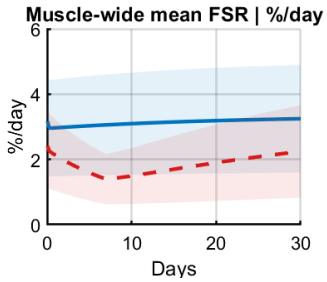


**Figure 4.** Simulated muscle-wide FSR (%/day). Whole lattice fractional synthesis rate was calculated using averaged individual fiber MPS rates. Model FSR rates in homeostasis and atrophy agree with the literature.

## Discussion

We present a fiber-type resolved agent-based model of murine disuse atrophy that has been partially calibrated using gastrocnemius unloading data within the CaliPro framework. The model integrates mechanical load, IGF-1, amino acids, and myostatin to regulate protein turnover and includes a time-varying anabolic resistance term that progressively blunts anabolic sensitivity during disuse. Although calibration is ongoing, the current accepted parameter space already reproduces several biologically relevant features of unloading, including maintenance of homeostasis under load, fiber-type specific CSA loss during disuse, a marked fall in fractional synthesis rate, and only modest increases in breakdown. Taken together, these findings support the interpretation that suppression of MPS, rather than large, sustained elevation of MPB, is the dominant driver of disuse atrophy in the present model.

A central result of the current study is that the dominant regulators of fiber size differ between loaded and unloaded conditions. Under homeostasis, sensitivity to myostatin and amino acid signaling emerged as the strongest determinant of final CSA. Under unloading, however, the reference basal synthesis parameter MPS_IIA and the load-dependent suppression of breakdown became stronger predictors of final fiber size. Because MPS_IIA sets the basal synthesis scale for the other fiber types, its strong association with atrophy severity suggests that baseline turnover architecture is a major determinant of vulnerability to unloading. This observation is consistent with the hypothesis that fibers with higher basal synthesis and turnover capacity can experience greater net loss when anabolic support is withdrawn.

The simulated turnover outputs provide an additional mechanistic interpretation of the model's behavior. Muscle-wide FSR fell by

approximately 57% during disuse, from about 3.5%/day to 1.5%/day, whereas MPB rose only modestly. This agrees with experimental work indicating that disuse atrophy is driven largely by reduced synthesis rather than by dramatic, sustained increases in proteolysis. In this sense, the current model recapitulates a key biological feature of unloading despite its still-simplified representation of catabolic signaling.

The inability of exercise and amino acid supplementation to fully prevent unloading-induced muscle loss remains a major obstacle for spaceflight countermeasure development. Under normal loading conditions, both protein ingestion and mechanical activity can robustly stimulate MPS. During disuse, however, this response becomes blunted. The present model captures that behavior phenomenologically through a time-varying anabolic resistance term. While this representation is intentionally simplified, it provides a useful starting point for future mechanistic refinement. In later model iterations, anabolic resistance could be decomposed into explicit contributors such as reduced mechanosensitive signaling, impaired capillary support for nutrient delivery, altered insulin/IGF pathway sensitivity, or other signaling bottlenecks that limit the translation of extracellular anabolic stimuli into increased synthesis.

The model also has several important limitations. First, the spatial architecture is derived from a single segmented gastrocnemius cross-section. Although alternative fiber-type compositions could be used to approximate other muscles, the present geometry, fiber size relationships, and capillary layout remain gastrocnemius-specific. This limits direct generalization to muscles with distinct structure and loading history. Second, ECM remodeling is not yet represented dynamically. In vivo, ECM adapts during disuse to prevent excessive accumulation of extracellular space as fibers atrophy. Because the current model does not yet include active fibroblast-mediated remodeling, lattice morphology can develop non-physiologic ECM gaps during longer simulations. Third, the catabolic component of the model remains simplified, with MPB regulated primarily through load and amino acid effects rather than explicit inflammatory, ubiquitin-proteasome, calpain, or autophagic modules.

Despite these limitations, the current model provides a useful foundation for future expansion. Candidate additions include dynamic ECM remodeling, capillary regression and angiogenic regulation, explicit inflammatory signaling, and muscle-specific calibration of baseline loading levels. These additions would allow the framework to address why postural muscles such as the gastrocnemius and soleus undergo more severe unloading atrophy than more intermittently activated muscles such as the tibialis anterior or extensor digitorum longus. Longer-term fiber-type specific datasets, especially beyond day 14 of unloading, would also improve calibration precision and reduce uncertainty in late-phase trajectory predictions.

## Conclusion

This paper summarizes the development and partial calibration of a fiber-type resolved agent-based model of murine disuse atrophy. The model integrates extracellular mechanical load, IGF-1, amino acids, and myostatin to regulate protein turnover and simulate fiber-type specific changes in normalized CSA during unloading. Even before full convergence of the parameter space is achieved, the current accepted model space reproduces key qualitative and semi-quantitative features of disuse atrophy, including stable homeostasis under loaded conditions, marked suppression of MPS during unloading, and differential regulation of homeostatic versus atrophic fiber size. Further

sensitivity analysis suggests that the mechanisms controlling baseline muscle size are not identical to those governing preservation of muscle during disuse. With continued calibration refinement and future incorporation of additional biology, this framework has the potential to serve as a mechanistic platform for countermeasure development and hypothesis testing relevant to long-duration spaceflight.

**Acknowledgements**

This research was supported by the Virginia Space Grant Consortium Graduate Fellowship as well as the National Institute of Health Systems Biology and Data Sciences Training Grant (T32 LM012416).

## References


1. Baskin KK, Winders BR, Olson EN. Muscle as a "mediator" of systemic metabolism. *Cell Metab*. 2015;21(2):237-248. doi:10.1016/j.cmet.2014.12.021

2. Wolfe RR. The underappreciated role of muscle in health and disease. *Am J Clin Nutr*. 2006;84(3):475-482. doi:10.1093/ajcn/84.3.475

3. Howard EE, Pasiakos SM, Fussell MA, Rodriguez NR. Skeletal Muscle Disuse Atrophy and the Rehabilitative Role of Protein in Recovery from Musculoskeletal Injury. *Adv Nutr*. 2020;11(4):989-1001. doi:10.1093/advances/nmaa015

4. Hill AM, McPhail SM, Haines TP, et al. Falls After Hospital Discharge: A Randomized Clinical Trial of Individualized Multimodal Falls Prevention Education. *J Gerontol A Biol Sci Med Sci*. 2019;74(9):1511-1517. doi:10.1093/gerona/glz026

5. Riley DA, Ellis S, Giometti CS, et al. Muscle sarcomere lesions and thrombosis after spaceflight and suspension unloading. *J Appl Physiol Bethesda Md 1985*. 1992;73(2 Suppl):33S-43S. doi:10.1152/jappl.1992.73.2.S33

6. Riley DA, Thompson JL, Krippendorf BB, Slocum GR. Review of spaceflight and hindlimb suspension unloading induced sarcomere damage and repair. *Basic Appl Myol BAM*. 1995;5(2):139-145.

7. Sasaki H, Kasagi F, Yamada M, Fujita S. Grip strength predicts cause-specific mortality in middle-aged and elderly persons. *Am J Med*. 2007;120(4):337-342. doi:10.1016/j.amjmed.2006.04.018

8. Li R, Xia J, Zhang X, et al. Associations of Muscle Mass and Strength with All-Cause Mortality among US Older Adults. *Med Sci Sports Exerc*. 2018;50(3):458-467. doi:10.1249/MSS.0000000000001448

9. Comfort P, McMahon JohnJ, Jones PaulA, et al. Effects of Spaceflight on Musculoskeletal Health: A Systematic Review and Meta-analysis, Considerations for Interplanetary Travel. *Sports Med Auckl Nz*. 2021;51(10):2097-2114. doi:10.1007/s40279-021-01496-9

10. Brooks N, Cloutier GJ, Cadena SM, et al. Resistance training and timed essential amino acids protect against the loss of muscle mass and strength during 28 days of bed rest and energy deficit. *J Appl Physiol Bethesda Md 1985*. 2008;105(1):241-248. doi:10.1152/japplphysiol.01346.2007

11. Trappe S, Costill D, Gallagher P, et al. Exercise in space: human skeletal muscle after 6 months aboard the International Space Station. *J Appl Physiol Bethesda Md 1985*. 2009;106(4):1159-1168. doi:10.1152/japplphysiol.91578.2008

12. Goldberg AL. Protein synthesis during work-induced growth of skeletal muscle. *J Cell Biol*. 1968;36(3):653-658. doi:10.1083/jcb.36.3.653

13. Stein TP, Larina IM, Leskiv MJ, Schluter MD. [Protein turnover during and after extended space flight]. *Aviakosmicheskaia Ekol Meditsina Aerosp Environ Med*. 2000;34(3):12-16.

14. Vandenburgh H, Chromiak J, Shansky J, Del Tatto M, Lemaire J. Space travel directly induces skeletal muscle atrophy. *FASEB J*. 1999;13(9):1031-1038. doi:10.1096/fasebj.13.9.1031

15. Kamal KY, Trombetta-Lima M. Mechanotransduction and Skeletal Muscle

Atrophy: The Interplay Between Focal Adhesions and Oxidative Stress. *Int J Mol Sci*. 2025;26(6):6. doi:10.3390/ijms26062802

16. Roberts MD, McCarthy JJ, Hornberger TA, et al. Mechanisms of mechanical overload-induced skeletal muscle hypertrophy: current understanding and future directions. *Physiol Rev*. 2023;103(4):2679-2757. doi:10.1152/physrev.00039.2022

17. Lecker SH, Solomon V, Mitch WE, Goldberg AL. Muscle protein breakdown and the critical role of the ubiquitin-proteasome pathway in normal and disease states. *J Nutr*. 1999;129(1S Suppl):227S-237S. doi:10.1093/jn/129.1.227S

18. Glover EI, Phillips SM, Oates BR, et al. Immobilization induces anabolic resistance in human myofibrillar protein synthesis with low and high dose amino acid infusion. *J Physiol*. 2008;586(24):6049-6061. doi:10.1113/jphysiol.2008.160333

19. Roberson PA, Shimkus KL, Welles JE, et al. A time course for markers of protein synthesis and degradation with hindlimb unloading and the accompanying anabolic resistance to refeeding. *J Appl Physiol*. 2020;129(1):36-46. doi:10.1152/japplphysiol.00155.2020

20. Ye F, Mathur S, Liu M, et al. Overexpression of IGF-1 attenuates skeletal muscle damage and accelerates muscle regeneration and functional recovery after disuse. *Exp Physiol*. 2013;98(5):1038-1052. doi:10.1113/expphysiol.2012.070722

21. Criswell DS, Booth FW, DeMayo F, Schwartz RJ, Gordon SE, Fiorotto ML. Overexpression of IGF-I in skeletal muscle of transgenic mice does not prevent unloading-induced atrophy. *Am J Physiol*. 1998;275(3 Pt 1):E373-379. doi:10.1152/ajpendo.1998.275.3.e373

22. Swat MH, Thomas GL, Belmonte JM, Shirinifard A, Hmeljak D, Glazier JA. Multi-Scale Modeling of Tissues Using CompuCell3D. *Methods Cell Biol*. 2012;110:325-366. doi:10.1016/B978-0-12-388403-9.00013-8

23. Joslyn LR, Kirschner DE, Linderman JJ. CaliPro: A Calibration Protocol That Utilizes Parameter Density Estimation to Explore Parameter Space and Calibrate Complex Biological Models. *Cell Mol Bioeng*. 2021;14(1):31-47. doi:10.1007/s12195-020-00650-z

24. Haase M, Comlekoglu T, Petrucciani A, Peirce SM, Blemker SS. Agent-based model demonstrates the impact of nonlinear, complex interactions between cytokines on muscle regeneration. *eLife*. 2024;13. doi:10.7554/eLife.91924.1

25. Schneider CA, Rasband WS, Eliceiri KW. NIH Image to ImageJ: 25 years of image analysis. *Nat Methods*. 2012;9(7):671-675. doi:10.1038/nmeth.2089

26. Fitts RH, Trappe SW, Costill DL, et al. Prolonged space flight-induced alterations in the structure and function of human skeletal muscle fibres. *J Physiol*. 2010;588(18):3567-3592. doi:10.1113/jphysiol.2010.188508

27. Tsuji R, Fujita R, Hayashi T, et al. 0.33g mitigates muscle atrophy while 0.67g preserves muscle function and myofiber type composition in mice during spaceflight. *Sci Adv*. 2026;12(11):eaed2258. doi:10.1126/sciadv.aed2258

28. Goodman CA, Mabrey DM, Frey JW, et al. Novel insights into the regulation of skeletal muscle protein synthesis as revealed by a new nonradioactive in vivo technique. *FASEB J*. 2011;25(3):1028-1039. doi:10.1096/fj.10-168799

29. Goodman CA, Kotecki JA, Jacobs BL, Hornberger TA. Muscle fiber type-dependent differences in the regulation of protein synthesis. *PloS One*. 2012;7(5):e37890. doi:10.1371/journal.pone.0037890

30. Babcock LW, Knoblauch M, Clarke MSF. The role of myostatin and activin receptor IIB in the regulation of unloading-induced myofiber type-specific skeletal muscle atrophy. *J Appl Physiol Bethesda Md 1985*. 2015;119(6):633-642. doi:10.1152/japplphysiol.00762.2014

31. Bark TH, McNurlan MA, Lang CH, Garlick PJ. Increased protein synthesis after acute IGF-I or insulin infusion is localized to muscle in mice. *Am J Physiol-Endocrinol Metab*. 1998;275(1):E118-E123. doi:10.1152/ajpendo.1998.275.1.E118

32. Bloemberg D, Quadrilatero J. Rapid Determination of Myosin Heavy Chain Expression in Rat, Mouse, and Human Skeletal Muscle Using Multicolor Immunofluorescence Analysis. *PLOS ONE*. 2012;7(4):e35273. doi:10.1371/journal.pone.0035273

33. Tang K, Breen EC, Gerber HP, Ferrara NMA, Wagner PD. Capillary regression in vascular endothelial growth factor-deficient skeletal muscle. *Physiol Genomics*. 2004;18(1):63-69. doi:10.1152/physiolgenomics.00023.2004

34. Filion RJ, Popel AS. Intracoronary administration of FGF-2: a computational model of myocardial deposition and retention. *Am J Physiol-Heart Circ Physiol*. 2005;288(1):H263-H279. doi:10.1152/ajpheart.00205.2004

35. Martin KS, Blemker SS, Peirce SM. Agent-based computational model investigates muscle-specific responses to disuse-induced atrophy. *J Appl Physiol*. 2015;118(10):1299-1309. doi:10.1152/japplphysiol.01150.2014

36. Alford EK, Roy RR, Hodgson JA, Edgerton VR. Electromyography of rat soleus, medial gastrocnemius, and tibialis anterior during hind limb suspension. *Exp Neurol*. 1987;96(3):635-649. doi:10.1016/0014-4886(87)90225-1

37. Jang J, Park S, Kim Y, et al. Myostatin Inhibition-Induced Increase in Muscle Mass and Strength Was Amplified by Resistance Exercise Training, and Dietary Essential Amino Acids Improved Muscle Quality in Mice. *Nutrients*. 2021;13(5):1508. doi:10.3390/nu13051508

38. Pavis GF, Abdelrahman DR, Murton AJ, Wall BT, Stephens FB, Dirks ML. Short-term disuse does not affect postabsorptive or postprandial muscle protein fractional breakdown rates. *J Cachexia Sarcopenia Muscle*. 2023;14(5):2064-2075. doi:10.1002/jcsm.13284

39. Li G, Li Z, Liu J. Amino acids regulating skeletal muscle metabolism: mechanisms of action, physical training dosage recommendations and adverse effects. *Nutr Metab*. 2024;21:41. doi:10.1186/s12986-024-00820-0

40. Wang XH, Du J, Klein JD, Bailey JL, Mitch WE. Exercise ameliorates chronic kidney disease–induced defects in muscle protein metabolism and progenitor cell

function. *Kidney Int*. 2009;76(7):751-759. doi:10.1038/ki.2009.260

41. Harrison BC, Allen DL, Girten B, et al. Skeletal muscle adaptations to microgravity exposure in the mouse. *J Appl Physiol*. 2003;95(6):2462-2470. doi:10.1152/japplphysiol.00603.2003

42. Hanson AM, Stodieck LS, Cannon CMA, Simske SJ, Ferguson VL. Seven days of muscle re-loading and voluntary wheel running following hindlimb suspension in mice restores running performance, muscle morphology and metrics of fatigue but not muscle strength. *J Muscle Res Cell Motil*. 2010;31(2):141-153. doi:10.1007/s10974-010-9218-5

43. Rah B, Shafarin J, Qaisar R, Karim A, Hamad M, Muhammad JS. Mouse hindlimb unloading, as a model of simulated microgravity, leads to dysregulated iron homeostasis in liver and skeletal muscle cells. *Life Sci Space Res*. 2025;45:7-15. doi:10.1016/j.lssr.2025.01.003

44. Brocca L, Rossi M, Canepari M, Bottinelli R, Pellegrino MA. Exercise Preconditioning Blunts Early Atrogenes Expression and Atrophy in Gastrocnemius Muscle of Hindlimb Unloaded Mice. *Int J Mol Sci*. 2022;23(1):148. doi:10.3390/ijms23010148

45. Hanson AM, Young MH, Harrison BC, et al. Inhibiting myostatin signaling partially mitigates structural and functional adaptations to hindlimb suspension in mice. *Npj Microgravity*. 2023;9(1):1. doi:10.1038/s41526-022-00233-4

46. Cannavino J, Brocca L, Sandri M, Grassi B, Bottinelli R, Pellegrino MA. The role of alterations in mitochondrial dynamics and PGC-1α over-expression in fast muscle atrophy following hindlimb unloading. *J Physiol*. 2015;593(8):1981-1995. doi:10.1113/jphysiol.2014.286740

47. Xu Y, Zhang Z, Chen P, et al. Gait analysis for functional evaluation in a surgical hindlimb suspension model of muscle atrophy. *J Physiol*. n/a(n/a). doi:10.1113/JP289401

48. Bark TH, McNurlan MA, Lang CH, Garlick PJ. Increased protein synthesis after acute IGF-I or insulin infusion is localized to muscle in mice. *Am J Physiol-Endocrinol Metab*. 1998;275(1):E118-E123. doi:10.1152/ajpendo.1998.275.1.E118

49. Shimkus KL, Shirazi-Fard Y, Wiggs MP, et al. Responses of skeletal muscle size and anabolism are reproducible with multiple periods of unloading/reloading. *J Appl Physiol*. 2018;125(5):1456-1467. doi:10.1152/japplphysiol.00736.2017